Research Article | Vol. 32, No. 3 / 29 Jan 2024 / Optics Express 3480

Structured illumination ptychography and at-wavelength characterization with an EUV diffuser at 13.5 nm wavelength

WILHELM ESCHEN,[1,2,3,*] CHANG LIU,[1,2,3] MICHAEL STEINERT,[3] DANIEL S. PENAGOS MOLINA,[1,2,3] THOMAS SIEFKE,[3,4] UWE D. ZEITNER,[4,5] JÖRG KASPAR,[6] THOMAS PERTSCH,[1,2,3] JENS LIMPERT,[1,2,3,4] AND JAN ROTHHARDT[1,2,3,4]

[1] *Helmholtz-Institute Jena, Fröbelstieg 3, 07743 Jena, Germany*
[2] *GSI Helmholtzzentrum für Schwerionenforschung, Planckstraße 1, 64291 Darmstadt, Germany*
[3] *Institute of Applied Physics, Abbe Center of Photonics, Friedrich-Schiller-University Jena, Albert Einstein-Straße 15, 07745 Jena, Germany*
[4] *Fraunhofer Institute for Applied Optics and Precision Engineering, Albert-Einstein-Str. 7, 07745 Jena, Germany*
[5] *Munich University of Applied Sciences, Lothstr. 34, 80335 Munich, Germany*
[6] *Fraunhofer-Instutut for Material and Beam Technology, Winterbergstrasse 28, 01277 Dresden, Germany*
[*] *wilhelm.eschen@uni-jena.de*

Abstract: Structured illumination is essential for high-performance ptychography. Especially in the extreme ultraviolet (EUV) range, where reflective optics are prevalent, the generation of structured beams is challenging and, so far, mostly amplitude-only masks have been used. In this study, we generate a highly structured beam using a phase-shifting diffuser optimized for 13.5 nm wavelength and apply this beam to EUV ptychography. This tailored illumination significantly enhances the quality and resolution of the ptychography reconstructions. In particular, when utilizing the full dynamics range of the detector, the resolution has been improved from 125 nm, when using an unstructured beam, to 34 nm. Further, ptychography enables the quantitative measurement of both the amplitude and phase of the EUV diffuser at 13.5 nm wavelength. This capability allows us to evaluate the influence of imperfections and contaminations on its "at wavelength" performance, paving the way for advanced EUV metrology applications and highlighting its importance for future developments in nanolithography and related fields.

Published by Optica Publishing Group under the terms of the Creative Commons Attribution 4.0 License. Further distribution of this work must maintain attribution to the author(s) and the published article's title, journal citation, and DOI.

1. Introduction

Coherent diffractive imaging (CDI) is a computational microscopy technique that enables the reconstruction of a coherently illuminated object from its measured diffraction pattern [1]. Due to its lensless nature, CDI surpasses the limitations of image-forming lenses, which offers advantages, particularly in the X-ray range [2,3]. In recent years, ptychography [4,5], a scanning form of CDI, has emerged as an important CDI modality since it removes the restrictions on the lateral sample size. In ptychography, an object is scanned through an illuminating beam, which is referred to as probe, and diffraction patterns are recorded for overlapping positions. The resulting diverse set of diffraction patterns is then used to reconstruct the amplitude and phase of the object and probe by an iterative phase retrieval algorithm. Especially in the X-ray range at synchrotron facilities ptychography has emerged as an established method [6], due to its ability to overcome the limitations of X-ray optics. Consequently, ptychography has found widespread

#507715 https://doi.org/10.1364/OE.507715
Journal © 2024 Received 6 Oct 2023; revised 9 Nov 2023; accepted 15 Nov 2023; published 18 Jan 2024

Corrected 2 February 2024

applications, including non-destructive and high-resolution 3D imaging of various samples [7] and spectroscopic imaging [8].

At the same time, there has been a rapid improvement in the performance of ultrafast laser systems pushing the average power into the kilowatt range [9], facilitating the development of coherent extreme ultraviolet (EUV) sources based on high-order harmonic generation (HHG) [10]. These HHG sources can extend into the X-ray range [11] and generate a photon flux in the EUV spectral range that is comparable to that of synchrotron facilities [12]. Therefore, compact coherent EUV sources are available now, enabling experiments previously restricted to large-scale facilities [13]. Combining ptychography with state-of-the-art HHG sources allows high-resolution EUV imaging experiments to be realized on a lab scale [14,15].

EUV radiation offers several advantages for imaging. Firstly, the EUV spectral range provides excellent material contrast due to numerous electronic resonances within this spectral range. Furthermore, this spectral range provides multiple transmission windows that allow for penetration depths in the micrometer range for specific elements. In recent years, table-top EUV ptychography has enabled high-resolution imaging with sub-20 nm resolution [16]. The excellent material contrast provided by the EUV radiation has been utilized for both reflection [17,18] and transmission imaging [16] resulting in a wide range of applications including actinic metrology for the semiconductor industry [19–22] and high-resolution imaging of dry biological samples [23,24]. Further, ptychography has been widely used for high-resolution characterization of inherently broadband HHG sources [25–27] and EUV optical elements [28].

In EUV ptychography, the detector is typically placed close to the object to achieve a large detection numerical aperture (NA) and thus a high spatial resolution. However, so far mostly reflective optics were used to focus EUV radiation resulting in a small illumination NA. Nonetheless, it was observed that a wide angular illumination spectrum helps avoid artifacts in the reconstructed image and results in a higher image quality [29]. This is attributed to improved convergence of the iterative phase retrieval algorithms and relaxed dynamic range requirements. Consequently, the utilization of structured beams has been found beneficial [30,31]. This has recently been demonstrated in the EUV as well by placing a nanostructured binary mask in front of the object, which resulted in a highly structured orbital angular momentum (OAM) beam [16]. Further, it was recently shown that structured beams are especially important for achieving stable and high-quality image reconstruction for periodic objects [32].

The benefits of structured illumination in ptychography can be attributed to the convolution of the angular spectrum of the probe with the object's angular spectrum, which forms the diffraction pattern. For broad probe angular spectra, this results in diffraction patterns that are more evenly spread across the detector. As a result, the dynamic range requirements on the detector are relaxed. Further, plenty of features in the probe lead to more changes in the diffraction pattern when moving the sample, which adds more information to the ptychography dataset [33]. Certainly, the optimal illumination depends on the sample itself. However, a strongly structured illumination will be beneficial for samples with sparse structures and homogeneous areas (e.g. computer chips or EUV lithography mask). In this situation a diffusor, introducing randomized patterns on the sample and yielding highly spread diffraction patterns, promises significant advantages if employed as a beam shaping element for ptychography.

Phase-shifting diffusers are particularly beneficial as they can avoid a bright zero order in the diffraction pattern and are more photon-efficient than absorption-based diffusers due to their higher transmission. However, their usage has been so far limited to the visible [34] and hard X-ray range [35]. In the soft X-ray range, a random hole array based on an absorbing mask has been employed [31].

In contrast to previous experiments [16], that employed only binary, amplitude-only masks, this work introduces a phase-shifting EUV diffuser based on a nanostructured molybdenum mask. This diffuser shows significant performance improvements over state-of-the-art beam structuring

elements. To demonstrate this, a systematic study involving three different illuminations was conducted, which includes an unstructured beam, a structured beam generated by a binary mask, and a highly randomized speckle pattern generated by the introduced EUV diffuser. The diffuser spreads the diffraction pattern more evenly on the detector which enabled the measurement of 8 times more photons before saturation of the detector compared to an unstructured smooth beam. The performance of the different beams is tested on a sparse sample with a mixture of empty areas and structured features, similar to the features found in EUV lithography masks or integrated circuits. With this sample, the resolution improved from 125 nm to 34 nm when using the diffuser. This improvement can be attributed to the diffuser's effect of relaxing the detector's dynamic range requirements, which enabled the measurement of more photons with larger diffraction angles before overexposing the center of the detector. Additionally, ptychography was used to characterize the EUV diffuser in amplitude and phase at 13.5 nm wavelength, a task that is challenging with other metrology tools. The characterization revealed a phase and amplitude mismatch against the design values which can be attributed to chromium contamination that can be traced back to the manufacturing process. These results can be used in the future to improve the fabrication process.

2. Experimental setup and EUV diffuser design

The EUV ptychography setup consists of a fiber-laser-driven high-harmonic source generating a broadband spectrum reaching up to 100 eV. In short, the system employs a ytterbium-doped fiber laser with 75 kHz repetition rate and a central wavelength of 1030 nm. This laser is compressed, utilizing two noble-gas-filled hollow core fibers, to sub-10 fs pulses with a pulse energy of 0.4 mJ, yielding an average power of 30 W. These few-cycle pulses are then focused into a gas jet, where argon at a backing pressure of 600 mbar is used to generate high-order harmonics. This results in a broadband EUV continuum up to 100 eV, with a photon flux of 7×10^9 phot/s/eV at 13.5 nm wavelength. The EUV beam is then separated from the high-power driving laser using four grazing incidence plates. These plates predominantly reflect the EUV radiation while the IR laser is transmitted. Any residual laser light is blocked by two 200 nm zirconium filters. Three multilayer mirrors are used to image the EUV source on the sample and, at the same time, select a wavelength of 13.5 nm (92 eV) with a bandwidth of 0.23 nm from the broadband EUV continuum. The diffraction patterns are collected by a sCMOS detector placed 30 mm behind the sample. More details on the fiber-laser-driven HHG source [36], and the ptychography setup [16,37] have been recently published. For the ptychography measurements presented here 200 positions of a spiral scan pattern were used with a step size of 1000 nm. The ptychography measurements were reconstructed using the mPIE algorithm [38] employing 4 incoherent modes accounting for limited spatial coherence [39] and orthogonal probe relaxation accounting for a slight temporal drift [40]. The ptychography data sets were reconstructed employing the PtyLab toolbox [41].

Immediately before the sample (≈200 μm) a mask can be placed which is used to tailor the illuminating beam (Fig. 1 (a)). Here, one of three masks can be selected. In addition to the novel phase diffuser (Fig. 1 (d)), two amplitude-only masks are used here for comparison which have already been used in a previous study [16]. These masks can be used to generate an unstructured beam using a simple pinhole (Fig. 1 (b)) and a structured beam using a spiral-shaped mask (Fig. 1 (c)). The EUV diffuser is based on a randomized pixel pattern that introduces a π phase shift. To achieve this phase shift of π, we employ molybdenum with a thickness of 90 nm. Molybdenum is ideally suited as a phase-shifting material due to its high ratio of real part δ to imaginary part β of the refractive index at a wavelength of 13.5 nm ($\delta/\beta \approx 12$). Hence, 90 nm of molybdenum, without considering the Si_3N_4 membrane, yields a transmission of T≈0.58 [42]. A schematic sketch of the diffuser is shown in Fig. 1 (e).

The diffuser was manufactured in a two-step process. First, a pinhole with a diameter of 8 µm was etched through a 50 nm thick Si_3N_4 membrane which was subsequently coated with 200 nm

Optics EXPRESS

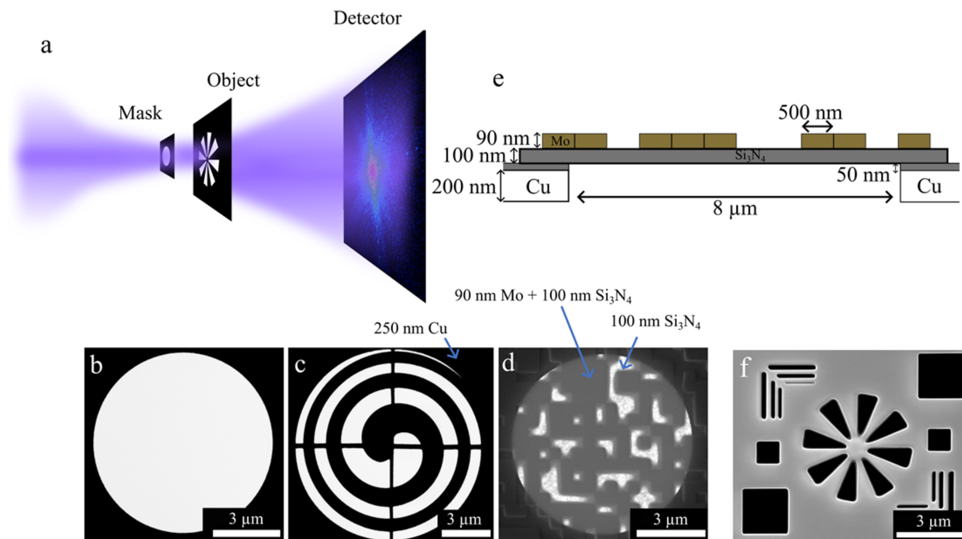

Fig. 1. (a) Schematical sketch of the setup. A beam-shaping mask is illuminated by an EUV beam. The transmission of the mask illuminates an object which is placed directly behind the object (≈200 *μm*). Subsequently, the diffraction pattern is recorded by a detector. (b) Transmission electron microscope (TEM) image of the pinhole used, yielding a smooth illumination. (c) TEM image of the spiral. (d) TEM image of the EUV diffuser. (e) Schematic cross-section of the EUV phase diffuser. (f) SEM image of the test sample.

of copper. The copper acts as an absorber and localizes the beam to a well-defined area. In the second step, electron beam lithography was used to expose a randomized checkerboard pattern on a 300 nm thick layer of FEP171 resist spin-coated on a layer-stack consisting of Cr (20 nm), Mo (90 nm), Si_3N_4 (100 nm), Cr (30 nm, top to bottom) on top of a 525 μm thick 100 mm Si wafer. The developed resist pattern was transferred into the Cr layer by means of Argon ion beam etching (IBE). Afterward, inductively coupled plasma reactive ion etching (ICP-RIE) was used to structure the underlying Mo layer. Now, the backside of this wafer was coated with 13 μm of AZ9260 positive tone photoresist and exposed with a pattern of circles (2 mm diameter). After development, the resist pattern was used as a mask to etch vias through the Si substrate by ICP-RIE stopping at the Cr layer. Subsequently, this layer was removed through the vias using reactive ion etching (RIE). The remaining Si_3N_4 membrane with the Mo diffuser was then placed on the prefabricated pinhole. For this purpose, an oversized patch was cut from the membrane using focused ion beam milling (FIB) and placed on top of the pinhole with a micro-manipulator needle. Finally, electron and ion beam-induced deposition (E/IBID) of platinum was used to fixate the edges of the patch to the pinhole surrounding the absorber.

3. Structured illumination for EUV ptychography

Using an illumination with a broad angular spectrum and small structures brings multiple advantages, which have been discussed previously [35]. However, for the sake of completeness, these advantages will be briefly described here. First, the use of structured and high-NA illumination results in a reduced depth of field. This effect arises from the rapid changes of the probe along the propagation direction due to propagation effects of the illuminating beam. As a result, the projection approximation will become less accurate and invalid for thicker samples. On the other hand, this also results in more depth information, which, in combination with

multi-slice algorithms [43], can result in an improved depth resolution [44]. However, the sample investigated here is sufficiently thin, and thus this effect is not the subject of this research.

Second, structured illumination stabilizes the numerical reconstruction process, yielding more reliable and consistent results. A beam with a structured wavefront distribution causes more changes in the diffraction patterns for neighboring scanning positions. This diversity in the measured diffraction patterns improves ptychography reconstructions as it facilitates the phase-retrieval algorithm to distinguish between object and probe. Previous studies have demonstrated that using an unstructured smooth beam can lead to the presence of artifacts in the reconstructed objects [29].

Finally, the measurement is limited by the achievable signal-to-noise ratio. Since the measured diffraction patterns can be described as a convolution of the object's angular spectrum with the angular spectrum of the probe, a broad probe angular spectrum results in a spatially distributed diffraction pattern. Hence the central diffraction peak is less bright relieving requirements on the dynamic range of the detector. Or, in turn, enables the measurement of more photons at larger spatial frequencies before reaching detector saturation improving the SNR. This in turn may improve the achievable spatial resolution.

To demonstrate these advantages, for each mask (i.e. pinhole, spiral, and phase diffuser) ptychography measurements were performed on a test sample (Fig. 1 (f)). The test sample consists of a 50 nm Si_3N_4 membrane coated with 500 nm of Silicon. Subsequently, test structures (e.g. elbow structures) were etched into the sample using a focused ion beam (FIB). The corresponding reconstructed most dominant probe modes are summarized in Fig. 2.

The reconstructed dominant probe modes for the pinhole, OAM beam, and EUV diffuser are shown in the object plane (Fig. 2 (a)–(c)) and back-propagated to the mask plane (Fig. 2(d)–(f)) in the first and second columns of Fig. 2. It is evident that the diffuser leads to a highly structured speckle pattern on the sample (Fig. 2(c)). The diffraction patterns of the illuminated masks are depicted in Fig. 2(g)–(i), obtained by moving the sample out of the beam path, thereby showing the angular spectrum of the corresponding illuminations. Notably, the EUV diffuser results in the broadest angular spectrum. The last column displays a single diffraction pattern selected from a ptychography measurement where the complete dynamic range (16-bit) for each measurement was used. The diffraction pattern was consistently chosen from the same position of the ptychography scan pattern and is located at the center of the sample (Fig. 1(f)). Due to the narrow angular spectrum of the pinhole, the corresponding diffraction pattern (Fig. 2(j)) only spans the center of the detector. However, when using the diffuser (Fig. 2(l)), photons are spread more evenly across the entire detector, enabling the measurement of significantly larger diffraction angles. Additionally, in the pinhole and OAM-beam measurements, only a single bright spot at the center of the diffraction pattern is observed (inset in Figs. 2(j) and 2(k)). In contrast, when employing the EUV diffuser multiple bright speckles are evident (inset Fig. 2(l)). As a result, a higher number of photons can be measured before the detector becomes overexposed, enabling the measurement of larger diffraction angles. Hence, the EUV diffuser most efficiently distributes the photons across the detector.

Optics EXPRESS

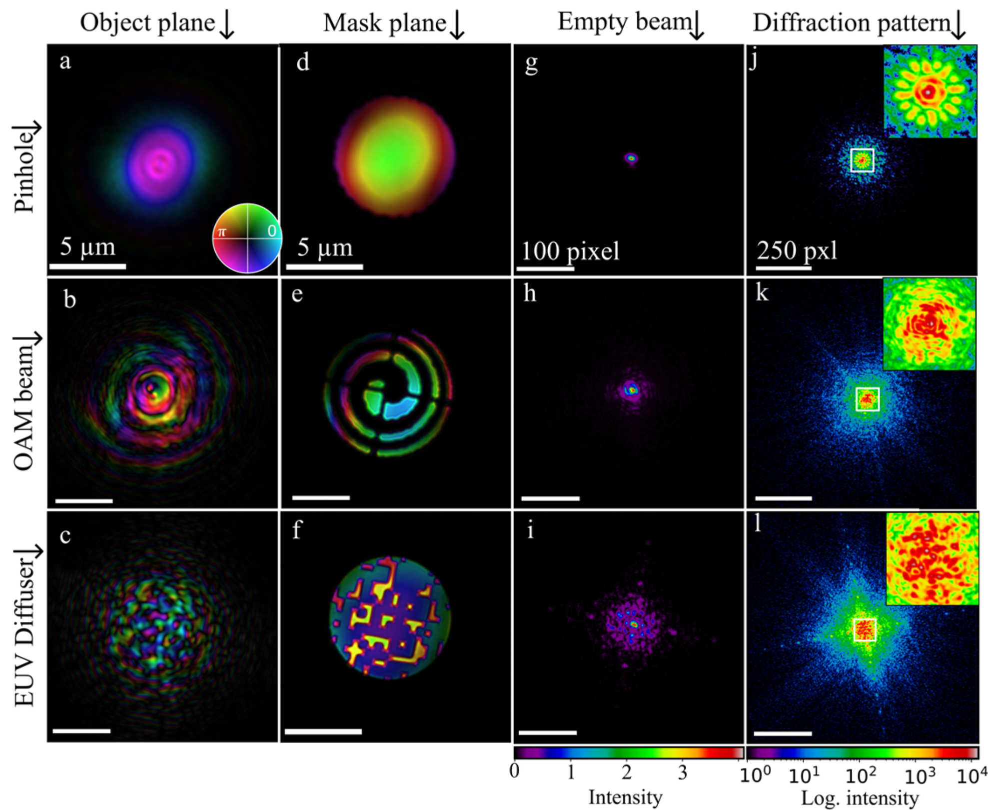

Fig. 2. Comparison of the reconstructed probes on the sample ((a)-(c)) and in the mask plane ((d)-(f)) for the pinhole, spiral, and EUV diffuser mask, respectively. (g)-(i) shows the far-field diffraction of each mask, which was measured by removing the sample. (j)-(l) shows a single diffraction pattern from the corresponding ptychography measurement showing that the EUV diffuser distributes the photons most evenly across the sample. The inset shows the enlarged central area of the diffraction pattern.

4. EUV ptychography using an EUV diffuser

In the next step, the impact of the different illuminations on the ptychographic image reconstruction is investigated. To accomplish this, three scenarios are examined. In the first scenario, the exposure time is kept constant for the three different illuminations. Since each mask has a different transmission, the dose on the sample differs for each illumination. An exposure time of 0.1 s was selected, as it represented the longest exposure time before the diffraction patterns captured using the pinhole mask became overexposed. The reconstructed complex transmission using the pinhole mask is depicted in Fig. 3(a) and shows artifacts at the elbow structure, which are not visible in the reconstructions using the spiral mask (Fig. 3(b)) and EUV diffuser (Fig. 3(c)). To evaluate the achieved resolution for each illumination a second ptychography scan was measured and the Fourier ring correlation was evaluated using the half-bit criterion (Fig. 3(d)). The results demonstrate that the OAM illumination yields the highest resolution with 77 nm, outperforming the smooth pinhole illumination (125 nm) and the EUV diffuser (114 nm). However, the EUV diffuser exhibits a significantly lower transmission compared to the other masks, resulting in a 79% lower dose on the sample compared to the pinhole. Despite this lower dose, the EUV

Optics EXPRESS

diffuser still achieved a higher resolution compared to the smooth illumination generated by the pinhole mask.

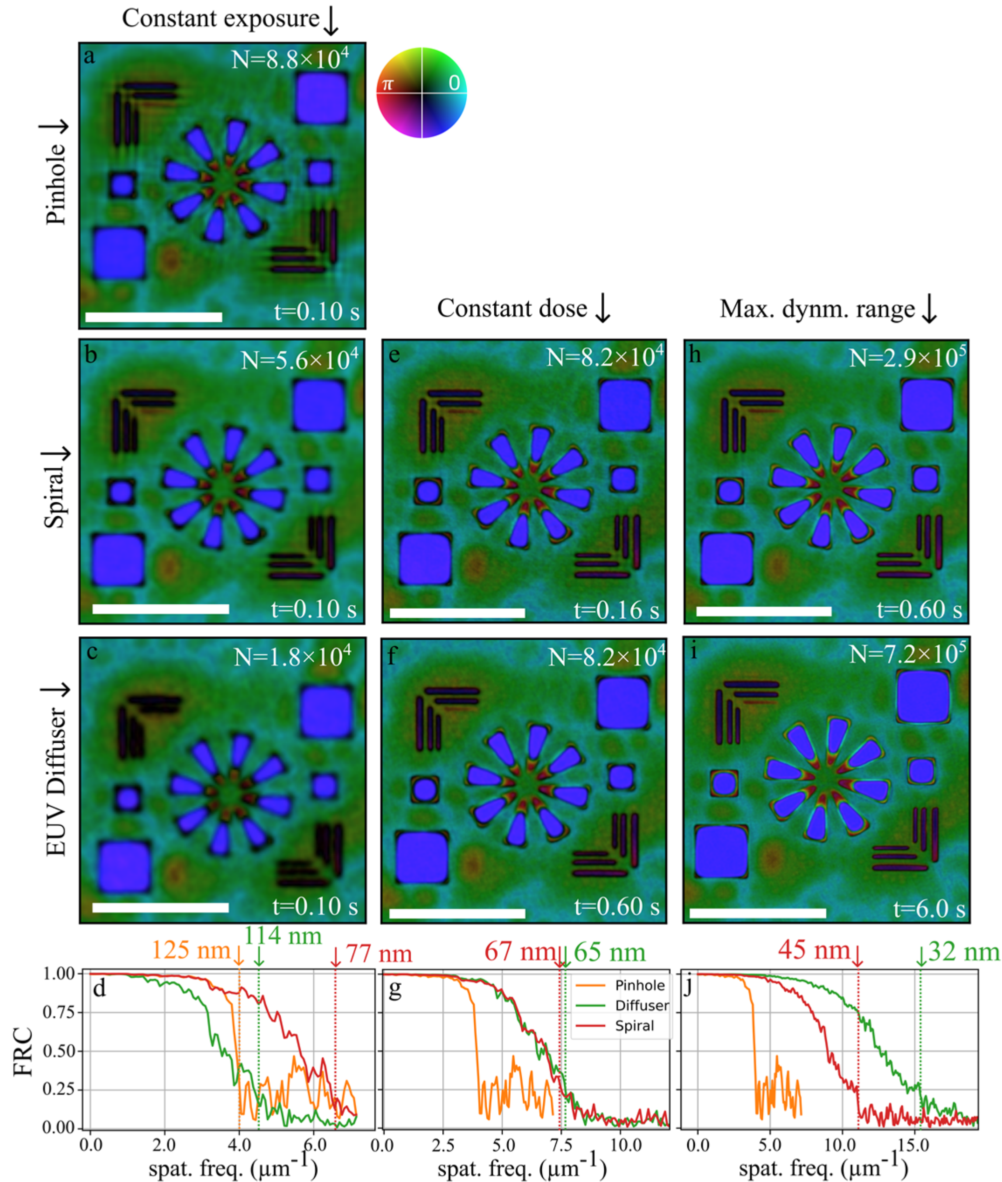

Fig. 3. Reconstructions of the test sample using a pinhole mask, spiral-shaped mask, and the EUV phase diffuser. The measurements were carried out for a constant exposure time of 0.1 s ((a)-(c)), constant dose ((e) and (f)), and using the maximal dynamic range of the detector ((h) and (i)). For each reconstruction, the averaged photon number N and the exposure time t are given by a label in the top-right and bottom-right corner, respectively. The half-pitch resolution for all these cases was evaluated by calculating the Fourier ring correlation (FRC) and using the half-bit criterion and is shown for the constant exposure time case, the constant dose case, and the maximal dynamic range case in (d), (g) and (j), respectively. The scale bar for all reconstructions corresponds to 5 μm.

In the second scenario, the exposure time for the OAM beam and EUV diffuser measurement was increased to 0.16 s and 0.60 s, respectively, yielding approximately the same number of photons measured with the detector. An averaged photon number of $\approx 8.8 \times 10^6$ photons per diffraction pattern was used for all three illuminations. The resulting reconstructions are shown in Fig. 3(e) and (f). The FRC yields a spatial half-pitch resolution of 67 nm for the spiral mask. Thus, the spatial resolution was significantly improved compared to the unstructured beam using the pinhole mask. The image quality gets even better, and the resolution is further increased to 65 nm when the EUV diffuser is utilized.

In the last scenario, the exposure time was increased to make use of the full 16-bit dynamic range of the detector. This allowed us to significantly increase the exposure time for the spiral and diffuser mask to 0.6 s and 6.0 s, respectively, while the exposure time for the pinhole was already limited by the saturation in the central peak of the diffraction patterns. A single diffraction pattern corresponding to each ptychography measurement is shown in Fig. 2(j)-(l). Due to the larger angular spectrum of the illumination, more photons have been detected without saturating the detector. Using the pinhole mask originally 8.8×10^4 photons per diffraction pattern were measured. However, with the spiral-shaped mask and the EUV diffuser, we recorded 2.9×10^5 photons and 7.2×10^5 photons, respectively, without reaching detector saturation. Therefore, the EUV diffuser allowed for 2.5 times more photons to be measured on the detector compared to the spiral mask before reaching overexposure. As a result, significantly larger diffraction angles are measured leading to a half-pitch resolution of 45 nm for the spiral mask and 32 nm for the EUV diffuser.

In general, the EUV diffuser showed the most substantial improvements when making use of the complete dynamic range of the detector. In this case, the spatial resolution was significantly improved from 125 nm (pinhole) and 45 nm (spiral-shaped mask) to 32 nm. However, this improvement came at the cost of a significantly increased exposure time due to a lower EUV transmission of the diffuser than expected. Consequently, this mismatch is investigated in more detail in the next section.

5. At-wavelength EUV diffuser characterization

The transmission of the EUV diffuser was measured to be 6 times lower than that of the pinhole. This difference cannot be fully explained by the known transmission properties of the utilized materials, which include a 100 nm Si_3N_4 membrane ($T \approx 0.42$) and a nanostructured 90 nm molybdenum layer ($T \approx 0.58$) with a fill-factor of approximately 0.5.

Utilizing ptychography, we have the unique ability to characterize the exit wave of the EUV diffuser in amplitude (Fig. 4(a)) and phase (Fig. 4(b)) at 13.5 nm wavelength. For this reason, a lineout is taken from the central structure which is shown in Fig. 4(c), and it is assumed that the wavefront of the illuminating beam is flat in the center of the aperture. The lineout reveals a phase shift of $\varphi \approx 3.4$ rad, and transmission of $T \approx 0.25$ for the nano-structured molybdenum. The observed transmission of $T \approx 0.25$ deviates strongly from the expected transmission of 90 nm Mo ($T \approx 0.58$). Furthermore, at the edges of the structure pronounced dips are apparent (indicated by a dotted circle in Fig. 4(c)), which look like low spatial frequency artifacts.

Motivated by the EUV measurements energy dispersive X-ray spectroscopy (EDX) measurements and SEM images of an identical replica, which were fabricated in the same run, were acquired. These results are shown in Fig. 4(f)-(j). The EDX measurements reveal a strong molybdenum signal along with a chromium signal. The presence of chromium was not expected and can be attributed to the manufacturing process where it was used as an etching barrier and indicates that the chromium was not removed after fabrication.

Under the assumption that the EUV diffuser contains only molybdenum and chromium the reconstructed EUV phase (Fig. 4(a)) and amplitude (Fig. 4(b)) can be used to calculate the spatially resolved atomic density (given in atoms per area unit) for both materials. For a detailed

Optics EXPRESS

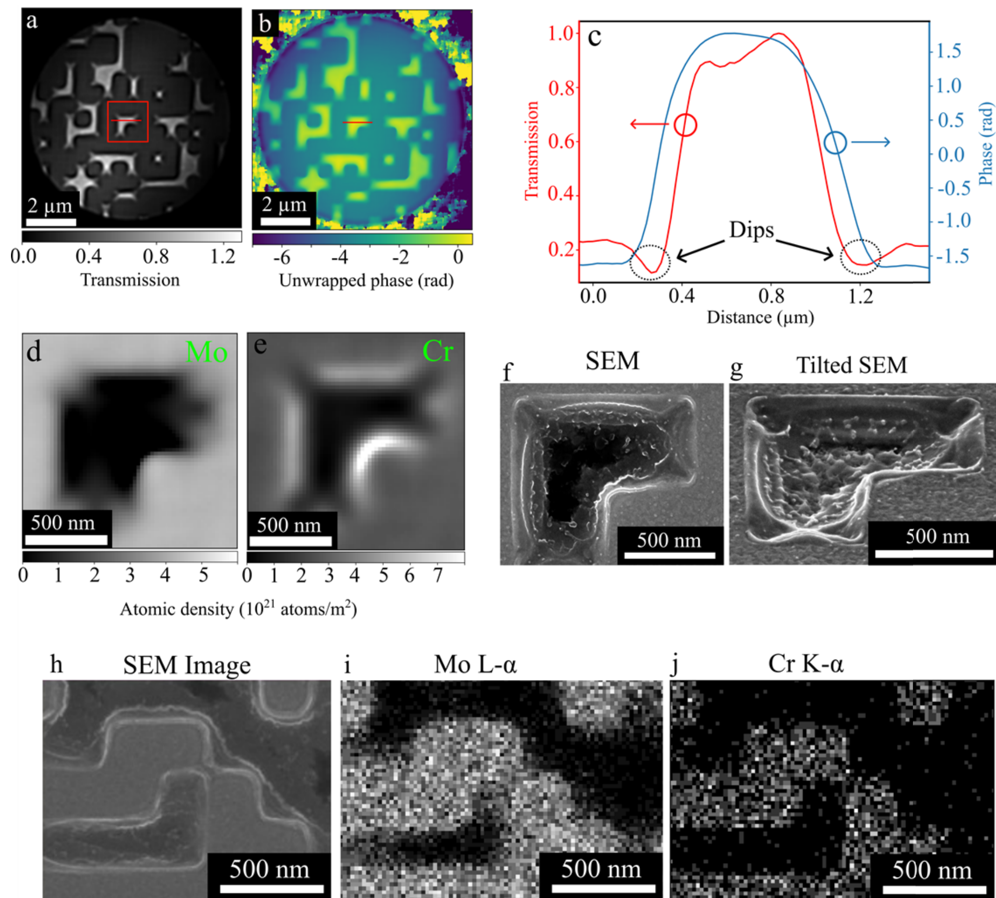

Fig. 4. Reconstructed transmission (a) and unwrapped phase (b) of the EUV phase diffuser. (c) Lineout of the transmission and phase indicated in (a) and (b) by a red line. (d) and (e) show the atomic density in atoms/m^2 of molybdenum and chromium calculated from the reconstructed phase and amplitude. (f) and (g) shows SEM images of the same structure of a replica that was produced in the same run where for (g) the sample was tilted. (h) shows another position at the replica where an EDX measurement was performed showing molybdenum (i) and chromium (j).

Optics EXPRESS

derivation of the calculation of the atomic densities, please refer to the Supplement 1. The extracted molybdenum and chromium maps for the central structure are shown in Fig. 4(d) and (e). The analysis reveals that there is a chromium layer covering the molybdenum structures with approximately 2.5×10^{21} atoms/m^2, which corresponds to a thickness of 30 nm, assuming a mass density of 7.14 g/cm^3. Further, at the edges of the structure additional chromium accumulated due to the IBE etching of the chromium layer which we believe also explains the dip shown in Fig. 4(c). The characteristic shape of the chromium contamination can also be recognized in the SEM images (Fig. 4(f) and (g)) indicating that the dips shown in Fig. 4 (c) can be attributed to real contaminations and do not represent numerical artifacts. However, the SEM images do not reveal the material composition. It should be noted that even these thin layers of chromium lead to a strong signal in amplitude and phase. Hence, EUV radiation proves to be ideally suited for resolving extremely thin chromium contaminations.

6. Discussion

In summary, an EUV phase diffuser was introduced for a wavelength of 13.5 nm. This was achieved by utilizing a Si_3N_4 membrane nanostructured with a randomized molybdenum pattern. The diffuser was used for ptychographic imaging of an artificially created sample containing empty areas and nano-structured features. On this sample a systematic analysis was carried out comparing the EUV diffuser to a smooth beam created by a pinhole and a structured beam created by an amplitude-only mask. The EUV diffuser led to a diffuse speckle pattern on the sample which resulted in a higher translation diversity and a broader angular spectrum – both advantageous attributes for ptychography. The broader angular spectrum facilitated the measurement of more photons before the detector was oversaturated. Consequently, this resulted in a resolution of 32 nm which is a significant improvement compared to the pinhole (125 nm) and the spiral-shaped mask (45 nm).

However, the diffuser exhibited a low transmission leading to longer exposure times. Characterization of the EUV reconstruction of the diffuser showed that the amplitude and phase of the molybdenum structures did not match the design values. This mismatch can be attributed to chromium contamination. Using a two-material model on the reconstructed EUV amplitude and phase of the diffuser, we created a 2-D map detailing the contamination distribution and its atomic density. Notably, this map showed accumulations of chromium at the edges of the diffuser structures. These characteristic features were confirmed by SEM images. Using EUV radiation even slight contaminations of chromium can be detected without destroying the sample demonstrating the effectiveness of at-wavelength metrology for critical optical components. Our findings showcase the significant potential of this approach for advanced EUV metrology applications and highlight its importance for future developments in nanolithography and related fields.

In the future, the diffuser fabrication process will be optimized in terms of phase shift and transmission by using feedback from the at-wavelength EUV diffuser. This will allow us to avoid chromium contaminations and precisely adjust the molybdenum thickness to attain a phase shift of π, enhancing both its transmission and angular spectrum. We expect that, in combination with a thinner Si_3N_4 membrane (e.g. 20 nm), the transmission can be improved by a factor of 3.

We believe that the EUV diffuser introduced here paves the way for several applications. The EUV phase diffuser can be integrated with a special mask designed for reflection ptychography [22]. This combination facilitates at-wavelength inspection of EUV lithography masks and other critical components. In particular, the investigation of highly periodic patterns benefits from structured illumination [32]. The presented diffuser also opens the route for other imaging modalities including speckle-based phase imaging [45] and single-shot coherent imaging based on randomized illuminations [46,47].

Optics EXPRESS

Funding. Freistaat Thüringen (41-5507-2016); Thüringer Aufbaubank (FKZ: 2019 FGI 0013); European Union's Horizon 2020 Framework Programme (20IND04 ATMOC, 20FUN02 POLight); International Research Training Group Meta-ACTIVE (IRTG 2675, project ID 437527638); Deutsche Forschungsgemeinschaft (SFB 1375, project ID 398816777); Fraunhofer-Gesellschaft (Cluster of Excellence Advanced Photon Sources); Thüringer Ministerium für Bildung, Wissenschaft und Kultur (2018 FGR 0080); Helmholtz Association (FISCOV, Ptychography 4.0, ZT-I-PF-4-018 AsoftXm).

Acknowledgments. The fabrication of the diffuser within this work was partly carried out by the microstructure technology team at IAP Jena. The authors would like to thank them for providing the fabrication facilities, carrying out processes, and providing support. The test sample used for the characterization was PVD coated by Erik Pflug from the Fraunhofer Institute for Material and Beam Technology. Portions of this work were presented at the Computational Optical Sensing and Imaging conference in 2023 under the title 'High-performance EUV Ptychography at 13.5 nm' (CM4B.6).

Disclosures. The authors declare no conflicts of interest.

Data availability. Data underlying the results presented in this paper are available at Zenodo [48].

Supplemental document. See Supplement 1 for supporting content.

References

1. J. R. Fienup, "Phase retrieval algorithms: a comparison," Appl. Opt. **21**(15), 2758 (1982).
2. J. Miao, T. Ishikawa, I. K. Robinson, *et al.*, "Beyond crystallography: Diffractive imaging using coherent X-ray light sources," Science **348**(6234), 530–535 (2015).
3. H. N. Chapman and K. A. Nugent, "Coherent lensless X-ray imaging," Nat. Photonics **4**(12), 833–839 (2010).
4. P. Thibault, M. Dierolf, A. Menzel, *et al.*, "High-resolution scanning x-ray diffraction microscopy," Science **321**(5887), 379–382 (2008).
5. A. M. Maiden and J. M. Rodenburg, "An improved ptychographical phase retrieval algorithm for diffractive imaging," Ultramicroscopy **109**(10), 1256–1262 (2009).
6. F. Pfeiffer, "X-ray ptychography," Nat. Photonics **12**(1), 9–17 (2018).
7. M. Dierolf, A. Menzel, P. Thibault, *et al.*, "Ptychographic X-ray computed tomography at the nanoscale," Nature **467**(7314), 436–439 (2010).
8. D. A. Shapiro, S. Babin, R. S. Celestre, *et al.*, "An ultrahigh-resolution soft x-ray microscope for quantitative analysis of chemically heterogeneous nanomaterials," Sci. Adv. **6**(51), eabc4904 (2020).
9. C. Grebing, M. Müller, J. Buldt, *et al.*, "Kilowatt-average-power compression of millijoule pulses in a gas-filled multi-pass cell," Opt. Lett. **45**(22), 6250 (2020).
10. M. Ferray, A. L'Huillier, X. F. Li, *et al.*, "Multiple-harmonic conversion of 1064 nm radiation in rare gases," J. Phys. B: At., Mol. Opt. Phys. **21**(3), L31–L35 (1988).
11. T. Popmintchev, M. C. Chen, D. Popmintchev, *et al.*, "Bright coherent ultrahigh harmonics in the kev x-ray regime from mid-infrared femtosecond lasers," Science **336**(6086), 1287–1291 (2012).
12. R. Klas, A. Kirsche, M. Gebhardt, *et al.*, "Ultra-short-pulse high-average-power megahertz-repetition-rate coherent extreme-ultraviolet light source," PhotoniX **2**(1), 4–8 (2021).
13. R. L. Sandberg, A. Paul, D. A. Raymondson, *et al.*, "Lensless diffractive imaging using tabletop coherent high-harmonic soft-X-ray beams," Phys. Rev. Lett. **99**(9), 098103 (2007).
14. M. D. Seaberg, B. Zhang, D. F. Gardner, *et al.*, "Tabletop nanometer extreme ultraviolet imaging in an extended reflection mode using coherent Fresnel ptychography," Optica **1**(1), 39 (2014).
15. B. Zhang, D. F. Gardner, M. D. Seaberg, *et al.*, "High contrast 3D imaging of surfaces near the wavelength limit using tabletop EUV ptychography," Ultramicroscopy **158**, 98–104 (2015).
16. W. Eschen, L. Loetgering, V. Schuster, *et al.*, "Material-specific high-resolution table-top extreme ultraviolet microscopy," Light: Sci. Appl. **11**(1), 117 (2022).
17. E. R. Shanblatt, C. L. Porter, D. F. Gardner, *et al.*, "Quantitative Chemically Specific Coherent Diffractive Imaging of Reactions at Buried Interfaces with Few Nanometer Precision," Nano Lett. **16**(9), 5444–5450 (2016).
18. M. Tanksalvala, C. L. Porter, Y. Esashi, *et al.*, "Nondestructive, high-resolution, chemically specific 3D nanostructure characterization using phase-sensitive EUV imaging reflectometry," Sci. Adv. **7**(5), 9667–9694 (2021).
19. D. G. Lee, Y. W. Kim, S. Moon, *et al.*, "Effect of wrinkles on extreme ultraviolet pellicle reflectivity and local critical dimension," Appl. Opt. **61**(20), 5965–5971 (2022).
20. B. Wang, N. Brooks, M. Tanksalvala, *et al.*, "Robust and reliable actinic ptychographic imaging of highly periodic structures in EUV photomasks," in Https://Doi.Org/10.1117/12.2641726, B. S. Kasprowicz and T. Liang, eds. (SPIE, 2022), 12293, p. 50.
21. Y. Nagata, T. Harada, T. Watanabe, *et al.*, "At wavelength coherent scatterometry microscope using high-order harmonics for EUV mask inspection," Int. J. Extreme Manuf. **1**(3), 032001 (2019).
22. H. Lu, M. Odstrčil, C. Pooley, *et al.*, "Characterisation of engineered defects in extreme ultraviolet mirror substrates using lab-scale extreme ultraviolet reflection ptychography," Ultramicroscopy **249**, 113720 (2023).
23. P. D. Baksh, M. Ostrčil, M. Miszczak, *et al.*, "Quantitative and correlative extreme ultraviolet coherent imaging of mouse hippocampal neurons at high resolution," Sci. Adv. **6**(18), eaaz3025 (2020).

Optics EXPRESS

24. C. Liu, W. Eschen, L. Loetgering, *et al.*, "Visualizing the ultra-structure of microorganisms using table-top extreme ultraviolet imaging," PhotoniX **4**(1), 1–15 (2023).
25. M. Du, X. Liu, A. Pelekanidis, *et al.*, "High-resolution wavefront sensing and aberration analysis of multi-spectral extreme ultraviolet beams," Optica **10**(2), 255–263 (2023).
26. D. Goldberger, D. Schmidt, J. Barolak, *et al.*, "Spatiospectral characterization of ultrafast pulse-beams by multiplexed broadband ptychography," Opt. Express **29**(20), 32474 (2021).
27. B. Zhang, D. F. Gardner, M. H. Seaberg, *et al.*, "Ptychographic hyperspectral spectromicroscopy with an extreme ultraviolet high harmonic comb," Opt. Express **24**(16), 18745 (2016).
28. L. Loetgering, X. Liu, A. C. C. De Beurs, *et al.*, "Tailoring spatial entropy in extreme ultraviolet focused beams for multispectral ptychography," Optica **8**(2), 130 (2021).
29. M. Guizar-Sicairos, M. Holler, A. Diaz, *et al.*, "Role of the illumination spatial-frequency spectrum for ptychography," Phys. Rev. B **86**(10), 100103 (2012).
30. M. Odstrčil, M. Lebugle, M. Guizar-Sicairos, *et al.*, "Towards optimized illumination for high-resolution ptychography," Opt. Express **27**(10), 14981 (2019).
31. A. M. Maiden, G. R. Morrison, B. Kaulich, *et al.*, "Soft X-ray spectromicroscopy using ptychography with randomly phased illumination," Nat. Commun. **4**(1), 1669 (2013).
32. B. Wang, N. J. Brooks, P. Johnsen, *et al.*, "High-fidelity ptychographic imaging of highly periodic structures enabled by vortex high harmonic beams," Optica **10**(9), 1245 (2023).
33. J. Rodenburg and A. Maiden, "Ptychography," in *Springer Handbook of Microscopy*, P. W. Hawkes and J. C. H. Spence, eds. (Springer International Publishing, 2019), pp. 819–904.
34. A. M. Maiden, J. M. Rodenburg, and M. J. Humphry, "Optical ptychography: a practical implementation with useful resolution," Opt. Lett. **35**(15), 2585 (2010).
35. P. Li, D. J. Batey, T. B. Edo, *et al.*, "Multiple mode x-ray ptychography using a lens and a fixed diffuser optic," J. Opt. **18**(5), 054008 (2016).
36. R. Klas, W. Eschen, A. Kirsche, *et al.*, "Generation of coherent broadband high photon flux continua in the XUV with a sub-two-cycle fiber laser," Opt. Express **28**(5), 6188 (2020).
37. W. Eschen, C. Liu, D. Penagos Molina, *et al.*, "High-speed and wide-field nanoscale table-top ptychographic EUV imaging and beam characterization with a sCMOS detector," Opt. Express **31**(9), 14212–14224 (2023).
38. A. Maiden, D. Johnson, and P. Li, "Further improvements to the ptychographical iterative engine," Optica **4**(7), 736 (2017).
39. P. Thibault and A. Menzel, "Reconstructing state mixtures from diffraction measurements," Nature **494**(7435), 68–71 (2013).
40. M. Odstrcil, P. Baksh, S. A. Boden, *et al.*, "Ptychographic coherent diffractive imaging with orthogonal probe relaxation," Opt. Express **24**(8), 8360 (2016).
41. L. Loetgering, M. Du, D. Boonzajer Flaes, *et al.*, "PtyLab.m/py/jl: a cross-platform, open-source inverse modeling toolbox for conventional and Fourier ptychography," Opt. Express **31**(9), 13763 (2023).
42. B. L. Henke, E. M. Gullikson, and J. C. Davis, "X-Ray Interactions: Photoabsorption, Scattering, Transmission, and Reflection at E = 50-30,000 eV, Z = 1-92," At. Data Nucl. Data Tables **54**(2), 181–342 (1993).
43. A. M. Maiden, M. J. Humphry, and J. M. Rodenburg, "Ptychographic transmission microscopy in three dimensions using a multi-slice approach," J. Opt. Soc. Am. A **29**(8), 1606 (2012).
44. H. Öztürk, H. Yan, Y. He, *et al.*, "Multi-slice ptychography with large numerical aperture multilayer Laue lenses," Optica **5**(5), 601 (2018).
45. K. S. Morgan, D. M. Paganin, and K. K. W. Siu, "X-ray phase imaging with a paper analyzer," Appl. Phys. Lett. **100**(12), 124102 (2012).
46. A. L. Levitan, K. Keskinbora, U. T. Sanli, *et al.*, "Single-frame far-field diffractive imaging with randomized illumination," Opt. Express **28**(25), 37103–37117 (2020).
47. F. Zhang, B. Chen, G. R. Morrison, *et al.*, "Phase retrieval by coherent modulation imaging," Nat. Commun. **7**(1), 13367 (2016).
48. W. Eschen and J. Rothhardt, "Raw ptychography data for manuscript with title 'Structured Illumination Ptychography and At-wavelength Characterization with an EUV diffuser at 13.5 nm Wavelength' Creators ," Zenodo: Version 1.0, 6 October 2023, https://doi.org/10.5281/zenodo.8414391.

140.181.72.48 {ts '2024-02-15 07:49:26'}